remote sensing

MDPI

Article

A Refined Regional Model for Estimating Pressure, Temperature, and Water Vapor Pressure for Geodetic Applications in China

Junyu Li [1,2], Bao Zhang [1,*], Yibin Yao [1], Lilong Liu [2], Zhangyu Sun [1] and Xiao Yan [1]

[1] School of Geodesy and Geomatics, Wuhan University, Wuhan 430079, China; junyu_li@whu.edu.cn (J.L.); ybyao@whu.edu.cn (Y.Y.); 2014301610290@whu.edu.cn (Z.S.); xxyan@whu.edu.cn (X.Y.)

[2] College of Geomatics and Geoinformation, Guilin University of Technology, Guilin 541004, China; lllong99@glut.edu.cn

* Correspondence: sggzb@whu.edu.cn; Tel.: +86-158-0276-6684

Received: 13 April 2020; Accepted: 25 May 2020; Published: 27 May 2020



Abstract: Pressure, temperature, and water vapor pressure are basic meteorological parameters that are frequently required in Global Navigation Satellite System (GNSS) positioning/navigation and GNSS meteorology. Although models like Global Pressure and Temperature (GPT) and Global Pressure and Temperature 2 wet (GPT2w) were developed for these demands, their spatial resolutions are lower than 0.75° and temporal resolutions are below 6 h, which limits their achievement. The publication of European Centre for Medium-Range Weather Forecasts (ECMWF) ERA5 hourly 0.25° × 0.25° data offers the opportunity to lift this limitation. In this work, the ERA5 surface data are used to evaluate the temporal variabilities of pressure, temperature, and water vapor pressure in the area of China. We characterize their diurnal variations using hourly data and take into account their geographical variations by 0.25° × 0.25° grids. In addition, we improve the height corrections for the three parameters employing the ERA5 pressure level data. Through these efforts, we build a new regional model named Chinese pressure, temperature, and water vapor pressure (CPTw), which has the advanced resolution of 0.25° × 0.25° and temporal resolution of 1 h. We evaluate the performance using ERA5 data and radiosonde data compared with the approved GPT2w model. Results demonstrate that the accuracies of the new model are superior to the GPT2w model in all meteorological parameters. The validation with the radiosonde data shows RMS for pressure, temperature, and water vapor pressure of the CPTw model is reduced by 14.1%, 25.8%, and 4.8%, compared with that of the GPT2w model. The new model catches especially well the diurnal changes in pressure, temperature, and water vapor pressure, which have never been realized before. Since the CPTw model can provide accurate empirical pressure, temperature, and water vapor pressure for any time and location in China and its surrounding areas, it can not only meet the need of empirical meteorological parameters in real-time geodetic applications like GNSS positioning and navigation, but it is also useful for GNSS meteorology.

Keywords: GNSS positioning/navigation; GNSS meteorology; pressure; temperature; water vapor pressure; ECMWF ERA5

1. Introduction

The Global Navigation Satellite System (GNSS) radio signal undergoes delay and bending when traveling through the neutral atmosphere. This effect is known as the tropospheric delay and is one of the most significant error sources in GNSS positioning/navigation, hence it should be properly modeled and corrected. The tropospheric delay is usually modeled by the delay in the zenith multiplied by a

mapping function. The zenith delay is divided into two components, namely the zenith hydrostatic delay (ZHD) and the zenith wet delay (ZWD) [1]. In high-precision analysis of geodetic observations, including GNSS and very long baseline interferometry (VLBI), accurate a priori ZHDs must be employed [2,3]. The need for ZHDs usually turns into the need for pressure since ZHD can be determined with in situ pressure observations in mm-level accuracy [4,5]. ZWDs are usually treated as unknown parameters and estimated in the analysis of geodetic observations. Unfortunately, a few real-time technologies do not have the advantage of postprocessing analyses, and thus necessitate the accessibility of accurate a priori ZWDs [6]. The ZWD can be approximated at centimeter level using the Saastamoinen model and surface temperature and water vapor pressure observations [4]. In addition, in GNSS meteorology, the determination of precipitable water vapor (PWV) from ZWD needs the weighted mean temperature (Tm), which is the unique parameter to convert ZWD to PWV and its determination needs surface temperature [7]. Therefore, surface pressure, temperature, and water vapor pressure are required in geodetic and meteorologic applications. However, not all the GNSS stations are equipped with automatic meteorological devices [8–11]. This causes the demand for empirical models. Especially in the past years when real-time GNSS applications have developed so rapidly [12], it increased the need for accurate empirical models [13].

Boehm et al. [3] established the Global Pressure and Temperature (GPT) model based on the European Centre for Medium-Range Weather Forecasts (ECMWF) ERA-40 data. This model uses a spherical harmonic function with degree nine and order nine (resolution is $20° \times 20°$) to represent global pressure and temperature fields and also considers their annual variations. The GPT model is widely used to provide empirical pressure and temperature in GNSS positioning/navigation and GNSS meteorology [14–17]. Lagler et al. [18] updated the GPT model to the GPT2 model by using the ECMWF ERA-Interim data and enhanced the model resolution to $5° \times 5°$. In addition to a better data source and improved spatial resolution, the GPT2 model considers the semiannual variations of pressure and temperature, and also outputs the lapse rates for temperature and water vapor pressure. Bohm et al. [6] published the GPT2w model that adds Tm and water vapor pressure decrease factor to the output parameters and has a higher resolution of $1° \times 1°$ compared to the GPT2 model. The GPT2w model has become a canonical tool in GNSS positioning/navigation and GNSS meteorology [19–22]. Krueger et al. [23,24] proposed the TropGrid model that takes the diurnal variations of meteorological parameters into account and has a spatial resolution of $1° \times 1°$, but ignores the semiannual variations of meteorological parameters. Similar models (the TropGrid2 model [25], the ITG model [26], and the WHU_CPT model [27]) are also established.

Even as the empirical models listed above improve, they still have some drawbacks. First, data sources used to establish the models have limited temporal resolutions (as high as only 6 h), such a resolution is insufficient to fully capture diurnal variations in temperature, pressure, and water vapor pressure. Second, their highest spatial resolution is only $0.75° \times 0.75°$. This low spatial resolution may limit their performance. In 2016, the release of the fifth-generation of reanalysis data distributed by ECMWF (ERA5) provides the opportunity to address these drawbacks. The ERA5 reanalysis data have unprecedented temporal resolution (1 h) and spatial resolution (0.25°). This motivates and enables us to develop a new model that fully characterizes diurnal variations and improves the spatial resolution of current models.

This study uses state-of-the-art ERA5 reanalysis data to develop a refined pressure, temperature, and water vapor pressure model. Compared to the existing models (e.g., GPT, GPT2w, and WHU_CPT), this new model is featured by the highest temporal (semidaily) and spatial (0.25°) resolutions, and may also exhibit the best accuracy. Due to these advancements, this new model can provide high-quality empirical pressure, temperature, and water vapor pressure data for geodetic applications, and may therefore improve the accuracy of GNSS position/navigation and GNSS meteorology.

2. Study Area and Data

2.1. Study Area

The latitude range of the research area is from 15°N to 55°N and the longitude range is from 70°E to 135°E, which covers the entire China area. The ERA5 reanalysis data range and the distribution of the 80 radiosonde stations used are shown in Figure 1.

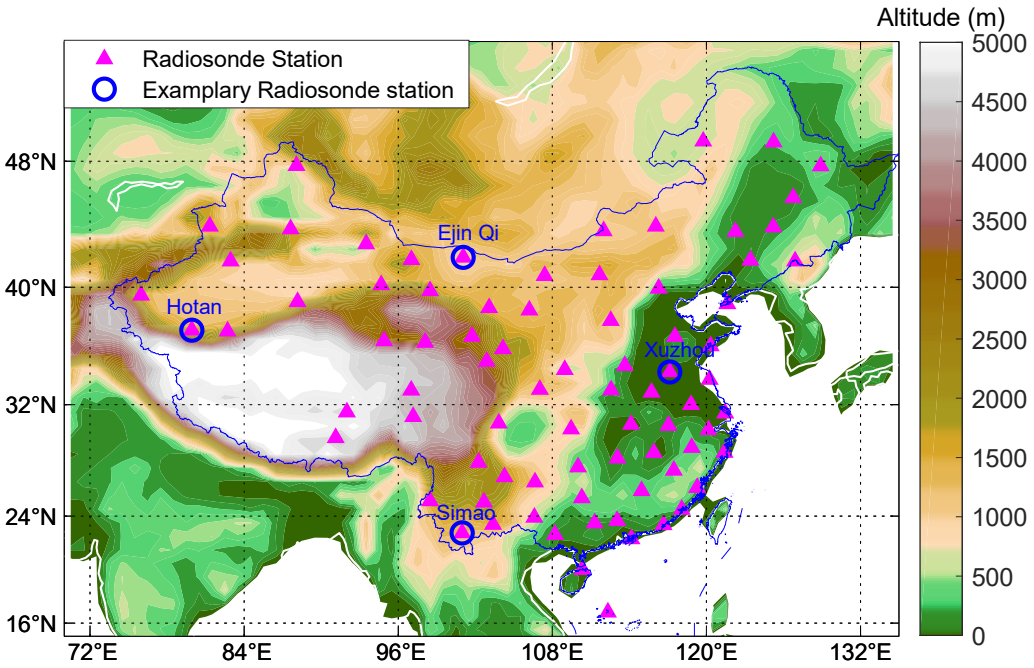

Figure 1. ERA5 reanalysis data range and distribution of the 80 radiosonde stations used.

2.2. ERA5 Reanalysis Data

ECMWF released the fifth-generation accurate global atmospheric reanalysis (ERA5) in 2018, which covers the period from 1979 to the present [28]. The ERA5 data have upgraded the spatial resolution to ~31 km and the temporal resolution to 1 h, in comparison with the earlier ERA-Interim data [29]. The ERA5 hourly data on pressure levels and hourly data on single levels in 2012–2017 are used in this work. The ERA5 hourly data on single levels is regard as "surface data" hereafter. The ERA5 surface data have a horizontal resolution of 0.25° × 0.25°. The ERA5 surface data, including geopotential, surface pressure, 2 m temperature, and 2 m dewpoint temperature, are used to model surface pressure, temperature, and water vapor pressure. We use the geopotential of the surface divided by gravity acceleration to represent the topography. The hourly data on pressure levels employed in this study have a horizontal resolution of 0.25° × 0.25° and a vertical resolution of 37 levels from 1000 to 1 hPa. The pressure level data, including geopotential, relative humidity, temperature, and pressure, are used to fit and solve parameters in the height corrections for temperature, pressure and water vapor pressure. Since the pressure level data do not provide water vapor pressure, we use the Wexler method [30,31] and temperature and relative humidity to calculate the water vapor pressure:

$$\ln e_{sv} = \sum_{i=0}^{3} c_i T^{i-1} + c_4 \ln T (273.15\ \mathrm{K} \le T < 373.15\ K) \quad (1)$$

$$\ln e_{sv} = \sum_{i=0}^{4} c_i T^{i-1} + c_5 \ln T (173.15\ \mathrm{K} \le T < 273.15\ K) \quad (2)$$

$$RH = \frac{e}{e_{sv}} \times 100\% \quad (3)$$

where e_{sv} denotes the saturated water vapor pressure (Pa) and T is temperature (K). In Equation (1), $c_0 = -6.04361117 \times 10^3$, $c_1 = 1.89318833 \times 10^1$, $c_2 = -2.8238594 \times 10^{-2}$, $c_3 = 1.7241129 \times 10^{-5}$, and $c_4 = 2.858487$. In Equation (2), $c_0 = -5.8653696 \times 10^3$, $c_1 = 2.224103300 \times 10^1$, $c_2 = 1.3749042 \times 10^{-2}$, $c_3 = -3.4031775 \times 10^{-5}$, $c_4 = 2.6967687 \times 10^{-8}$, and $c_5 = 6.918651 \times 10^{-1}$. RH is relative humidity in percent and e is the water vapor pressure. When we use dewpoint temperature to calculate water vapor pressure, we can directly obtain water vapor pressure by replacing T in Equations (1) and (2) by dewpoint temperature.

2.3. Radiosonde Data

Radiosonde is an accurate method to measure meteorological parameters and usually used to validate other observations and model outputs [32–36]. The radiosonde data are accessed freely from the archive at the website of the University of Wyoming (http://weather.uwyo.edu/upperair/sounding.html). These data are available at 00:00 UTC and 12:00 UTC every day. We downloaded all the available radiosonde data in the research area in 2017 and derived the temperature, pressure, and water vapor pressure. After removing 9 stations whose data quality was bad, 80 radiosonde stations were finally used and their distribution is shown in Figure 1.

3. Methods

To model the pressure, temperature, and water vapor pressure, we have to know their temporal and spatial variation features. As for the temporal variation, we mainly detect and determine its periodical variations. As for spatial variation, we separately describe its vertical and horizontal variations. We used 0.25° grids to describe the horizontal variations and used empirical models to describe the vertical variations. Therefore, determining the temporal and vertical variations of these parameters were the two key aspects in modeling them. The detailed steps for establishing the new model follow: Firstly, we used fast Fourier transform (FFT) analysis to detect the diurnal variations of pressure, temperature, and water vapor pressure based on the ERA5 data. Secondly, we determined the empirical models to describe the vertical variations of the three parameters and then used them to make height corrections. Finally, we determined the mathematical frames of the model and embodied it by determining its coefficients using ERA5 data. The schematic methodology for generating the CPTw is shown in Figure 2.

3.1. Diurnal Variations of Meteorological Parameters

The seasonal variations of pressure, temperature, and water vapor pressure have been extensively studied and modeled [6,18,23–25], but their diurnal variations are not well modeled due to insufficient temporal resolution of the data. Here we focus on analyzing the diurnal variations of the pressure, temperature, and water vapor pressure using the ERA5 data. We first fitted and removed the annual and semiannual signals by applying a high-pass filter to increase the signal-to-noise ratio of the diurnal signals. Then, a fast Fourier transform (FFT) analysis was executed on the residuals. Figure 3 shows the power spectrums at four typical points; we used 95% of the peak values to indicate the significance of the peaks.

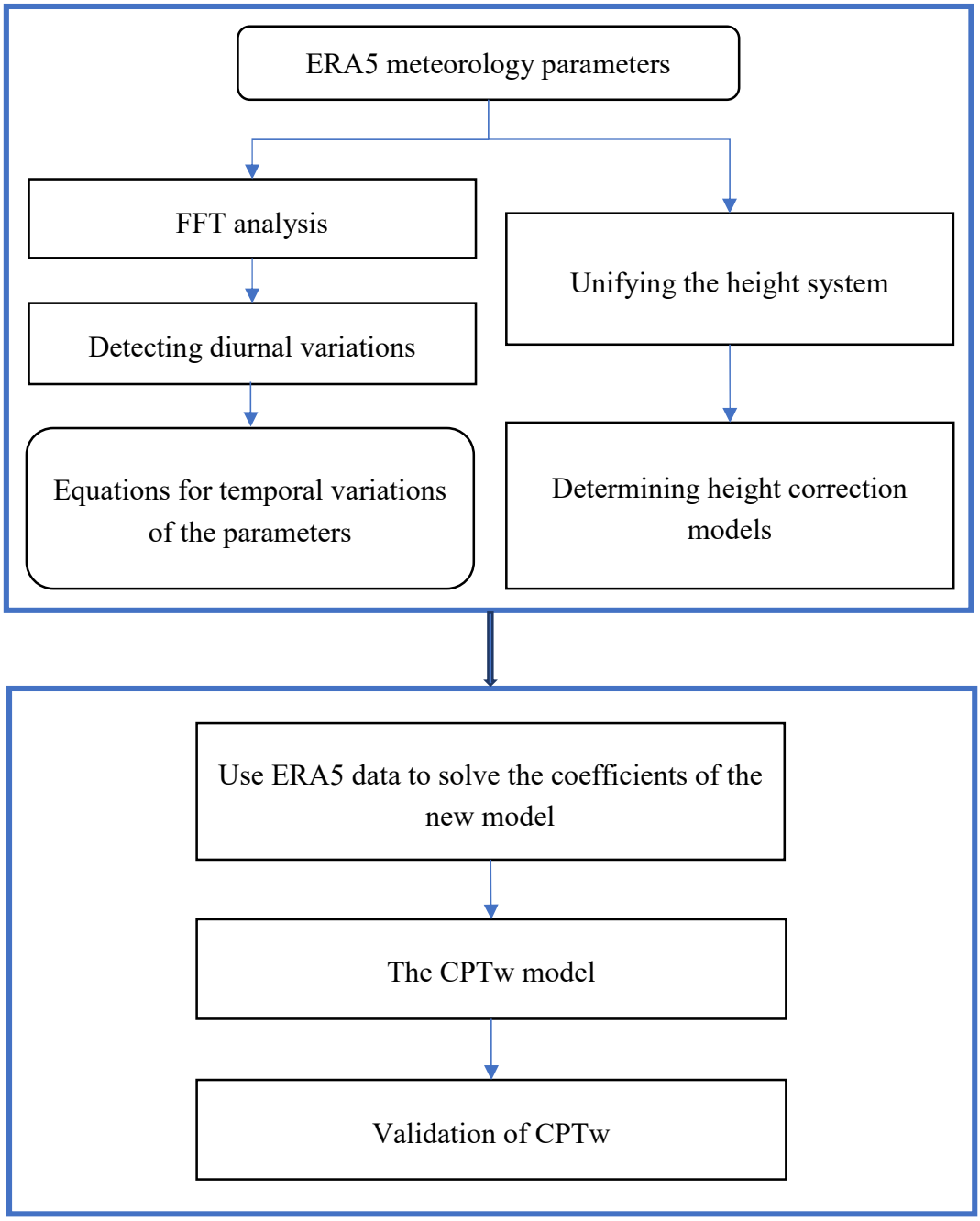

Figure 2. Flowchart of the main procedures to establish the CPTw model.

Two peaks are observed at 1 day and 0.5 day in the power spectrums of pressure (Figure 3a–d), suggesting that pressure has strong diurnal and semidiurnal variations. This is due to the atmospheric tides and was revealed by [37]. Especially, the peaks at 0.5 day are even greater, which displays that the semidiurnal variation is stronger than the diurnal variation. As for the temperature, two peaks are also observed at 1 day and 0.5 day (Figure 3a–d) but the 0.5-day peak is much weaker than the 1-day peak, which indicates that temperature has a forceful diurnal variation and a feeble semidiurnal variation. A peak from the power spectrum of water vapor pressure appears at 1 day in Figure 3b–d but does not appear in Figure 3a. Even when it has peaks at 1 day, the peaks are usually below the 95% level. The power spectrum of water vapor pressure does not show any peak at 0.5 day, indicating it has no regular semidiurnal variations. So, the diurnal variations of water vapor pressure are not as regular as the pressure and temperature, which present difficulties in modeling it.

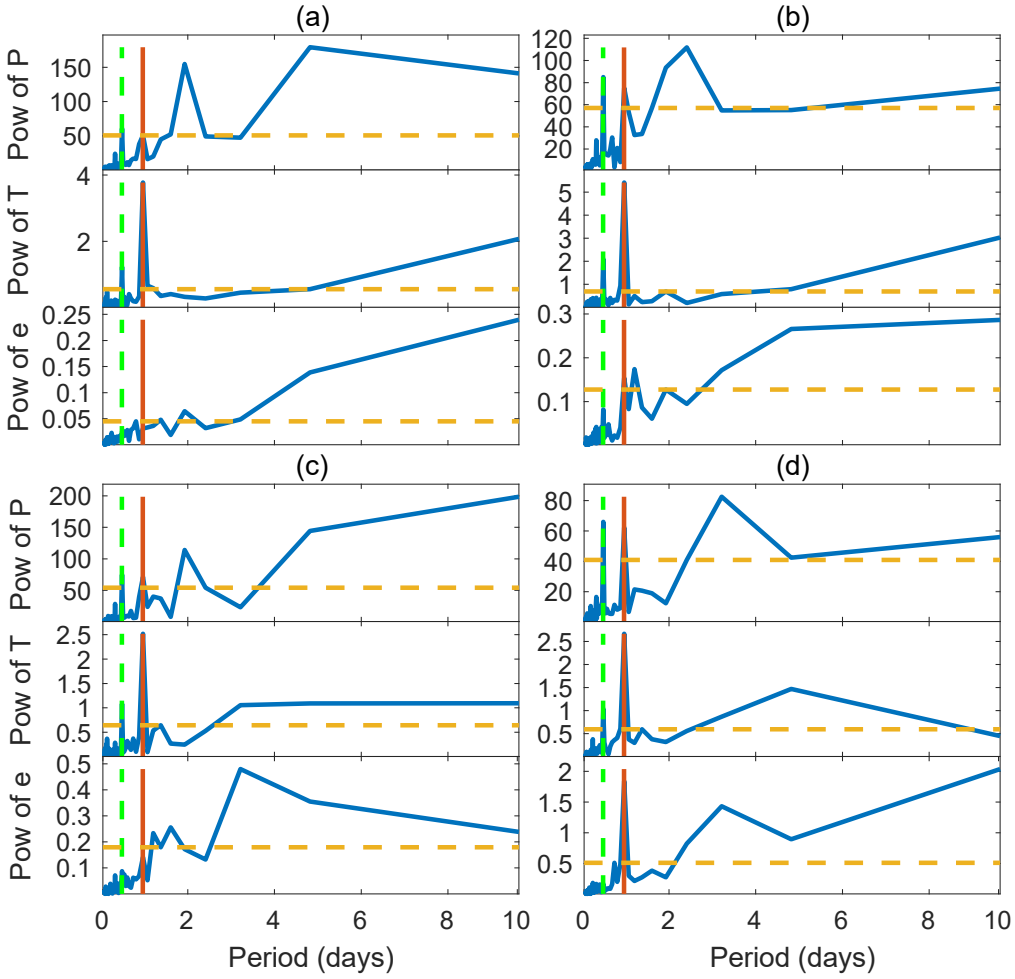

Figure 3. Power (Pow) spectrums of pressure (P), temperature (T), and water vapor pressure (e) at (**a**) (94.75°E, 37.5°N), (**b**) (88.75°E, 29°N), (**c**) (106°E, 35.5°N), and (**d**) (120.75°E, 23.5°N) from ERA5 grid data for 2012 to 2016. The horizontal dashed yellow lines indicate 95% of the peak values.

Based on the analysis above, we propose Equation (4) to express the diurnal and semidiurnal variabilities of pressure, temperature, and water vapor pressure:

$$r(t) = A_0 + A_1 \cos\left(\frac{HOD}{24} 2\pi\right) + B_1 \sin\left(\frac{HOD}{24} 2\pi\right) + A_2 \cos\left(\frac{HOD}{24} 4\pi\right) + B_2 \sin\left(\frac{HOD}{24} 4\pi\right) \quad (4)$$

where $r(t)$ could be pressure, temperature, or water vapor pressure, HOD indicates hour of day, and A_i and B_i ($i = 0,\ 1,\ 2$) are model coefficients. The second and third terms in Equation (4) together represent the diurnal variations and the fourth and fifth terms together represent the semidiurnal variations. When modeling water vapor pressure, the last two terms are not necessary.

3.2. Height Corrections for Temperature, Pressure, and Water Vapor Pressure

3.2.1. Height System Conversion

Since the GNSS uses the ellipsoid height system while the ERA5 data uses the geopotential height system, we needed to unify the height system so that we could determine the right height differences. Here we converted the geopotential height to the ellipsoid height by two steps. We first converted the geopotential height (it is the geopotential divided by gravity acceleration) to the orthometric height by using Equation (5) [38], and then converted the orthometric height to ellipsoid height by using

Equation (6). Unifying the height system is a premise for height corrections since height difference should be quantified in the same system.

$$\begin{cases} H_o = \frac{R_e(\varphi)\cdot H_g}{\frac{g(\varphi)}{g_0}R_e(\varphi)-H_g} \\ g(\varphi) = r_e\frac{1+k\sin^2\varphi}{\sqrt{1-e^2\sin^2\varphi}} \\ R_e(\varphi) = \frac{a}{1+f+m-2f\sin^2\varphi} \end{cases} \tag{5}$$

where φ is the latitude (radian), H_o and H_g are the orthometric height and geopotential height, $g(\varphi)$ is the gravity acceleration at φ, g_0 is the gravity constant (9.80665 m/s^2), and $R_e(\varphi)$ is the Earth's curvature radius at latitude φ. The variables a, f, m, k, e^2, r_e are constants and can be referred to [38].

$$H_e = H_o + N \tag{6}$$

where H_e is the ellipsoid height, N is the geoid height and was obtained from [39].

3.2.2. Determining Height Correction Methods for Meteorological Parameters

Determining the method for height correction is a critical aspect of modeling pressure, temperature, and water vapor pressure since these meteorological parameters show the strongest variations in the vertical direction. If proper consideration is given to their vertical changes, it will enable the model to provide accurate parameters at different heights.

The exponential function is commonly used to make height corrections for pressure [6,18,25,26]. The linear function is used to do height corrections for temperature [6,18,23–26]. For water vapor pressure, most studies employ the exponential function to do the height correction [6,23–25]. Accepting the conventional approaches, we used Equations (7), (10), and (13) to do the height corrections for pressure, temperature, and water vapor pressure, which are the same methods used in the GPT2w model.

$$P = P_0\cdot\exp\left(-\frac{g_0\cdot dMtr}{R_g\cdot T_v}\cdot dh\right) \tag{7}$$

$$T_v = T_0\cdot(1+0.6077\cdot Q) \tag{8}$$

$$Q = 0.622\cdot e_0/(P_0 - 0.378\cdot e_0) \tag{9}$$

where P refers to the pressure (hPa) at the site, P_0 represents the grid-based pressure (hPa) at the surface, dh denotes difference of height between site and grid point, $dMtr$ refers to the molar mass of dry air ($28.965\cdot10^{-3}$ kg/mol), R_g represents the universal gas constant (8.3143 J/K·mol), T_v is the virtual temperature (K), T_0 is the grid-based temperature (K) at two meters above the surface, Q denotes the specific humidity, and e_0 indicates the grid-based water vapor pressure (hPa) at two meters above the surface.

$$T = T_0 + \beta\cdot dh \tag{10}$$

where T refers to the temperature (K) at the site and β denotes the temperature lapse rate (K/km).

According to Smith [40], the water vapor mixing ratio ω can be well approximated by

$$\omega = \varepsilon\cdot(e/P) \tag{11}$$

where ε = 0.622. Smith [40] also assumes that the average decrease of moisture through the entire atmosphere column can be described by the power law:

$$\omega = \omega_0\cdot(P/P_0)^{\lambda} \tag{12}$$

where ω_0 is the surface water vapor mixing ratio.

Substituting Equation (11) into (12), we obtain

$$e = e_0 \cdot (P/P_0)^{\lambda+1} \tag{13}$$

where e refers to the water vapor pressure in hPa at the site; we follow [6] to call λ "the water vapor pressure decrease factor" which is the key parameter to describe the average vertical variation of water vapor pressure. λ can be obtained by fitting Equation (13) or (14) [41]. In this work, we follow [6] to solve λ by fitting Equation (14):

$$ZWD = 10^{-6} \cdot \left(k_2' + k_3/T_m\right) \frac{R_d}{(\lambda+1)g_0} e_0 \tag{14}$$

where k_2' and k_3 refer to empirically determined coefficients (16.52 K/hPa and 3.776×10^5 K^2/hPa), T_m denotes the weighted mean temperature (K), and R_d represents the specific gas constant for the dry constituents (287.058 J/kg·K) [42].

According to the Equations (7)–(14), β and λ are important parameters in height corrections for pressure, temperature, and water vapor pressure. The vertical profiles of pressure, temperature, and water vapor pressure from 2012 to 2016 were employed to fit and solve Equations (10) and (14) for β and λ. This was done hourly for consistency with the ERA5 data. Then, we performed a FFT analysis on the seasonal signals and their diurnal signals. Figure 4 shows the exemplary power spectrums of these at one grid point (88.75°E, 29°N). Two peaks are observed at 1 year and 0.5 year in Figure 4a,c and the peaks are all above the 95% level, suggesting that β and λ both have strong annual and semiannual variations. Especially, the peaks at 0.5 year from power spectrums are even greater than the peaks at 1 year, which demonstrates that semiannual variation of β is stronger than the annual variation. As for the diurnal power spectrums of β and λ, two peaks are also observed at 1 day and 0.5 day (Figure 4b,d) and all the peaks are greater than the 95% level, indicating β and λ also have diurnal and semidiurnal variation. Therefore, we consider not only the seasonal variations but also the diurnal variations of temperature lapse rate and the water vapor pressure decrease factor in height correction.

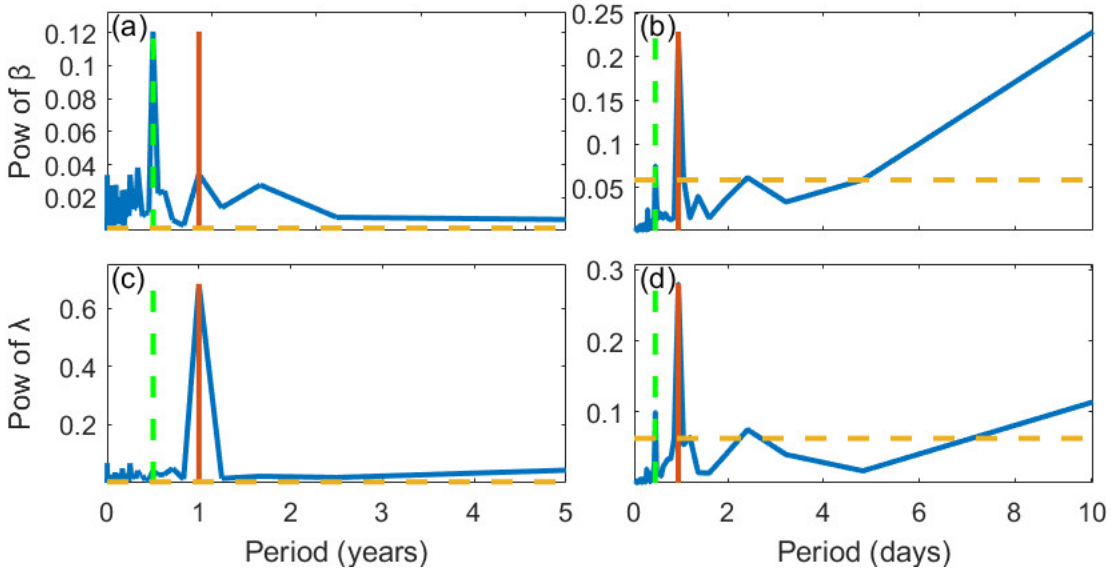

Figure 4. Power spectrums of β (**a**,**b**) and λ (**c**,**d**) at (88.75°E, 29°N). The left column shows the seasonal power spectrums. The right column shows the diurnal power spectrums. Data for this example are from ERA5 grid pressure level data from 2012 to 2016. The horizontal dashed yellow lines indicate the 95% of the peak values.

3.3. Establishing the CPTw Model

Since pressure, temperature, and water vapor pressure show obvious seasonal and diurnal variations, we use Equations (15) and (16) to represent their temporal variations.

$$MP = A_0 + A_1 \cos\left(\frac{HOD}{24}2\pi\right) + A_2 \sin\left(\frac{HOD}{24}2\pi\right) + A_3 \cos\left(\frac{HOD}{24}4\pi\right) + A_4 \sin\left(\frac{HOD}{24}4\pi\right) \quad (15)$$

$$A_i = a_{i0} + a_{i1} \cos\left(\frac{DOY}{365.25}2\pi\right) + a_{i2} \sin\left(\frac{DOY}{365.25}2\pi\right) + a_{i3} \cos\left(\frac{DOY}{365.25}4\pi\right) + a_{i4} \sin\left(\frac{DOY}{365.25}4\pi\right) \quad (16)$$

where *MP* indicates the meteorological parameters (pressure, temperature, or water vapor pressure). Equation (15) describes their diurnal variations, we fitted and solved coefficients A_i (i $= 0, \ldots, 4$) every day from 2012 to 2016. We used Equation (16) to fit A_i, which describes the seasonal variations of the meteorological parameters.

To account for geographic variations, Equations (15) and (16) were fitted and solved at each $0.25° \times 0.25°$ grid node in the research area. We also used similar methods to model the parameters β and λ in the height corrections and solved for the corresponding coefficients at the same grid nodes. It should be noted that since Equations (15) and (16) models only the annual mean and daily mean variations of pressure, temperature, and water vapor pressure, they cannot describe synoptic variations.

Equations (7)–(16) form the mathematical frame of the new model. Together with the determined coefficients on 0.25° grid nodes, they constitute a new model which is called the CPTw model. When using this model to estimate pressure, temperature, or water vapor pressure at any site, we first find the four grid nodes that are closest to the selected site and calculate the required parameters at the four grid nodes. Then we reduce the temperature, pressure, or water vapor pressure from grid-based height to the height of the site via height corrections. Finally, we interpolate the corrected temperature, pressure, or water vapor pressure to the site location through a bilinear interpolation. It should be noted that this model can perform well in the lower atmosphere (<10 km height), above which its performance may decrease.

3.4. Validation of CPTw

To assess the performance of the CPTw model, we exploit ERA5 data and the radiosonde data to validate the model and compare it to the widely used GPT2w model. Bias, standard deviation (STD), and root mean square (RMS) are used as the accuracy criteria. Bias, STD, and RMS are computed by Equations (17)–(19).

$$bias = \frac{1}{N}\sum_{i=1}^{N}\left(\widetilde{MP_i} - MP_i\right) \quad (17)$$

$$STD = \sqrt{1/N\sum_{i=1}^{N}(D_i - u)^2}; D_i = \widetilde{MP_i} - MP_i; u = 1/N\sum_{i=1}^{N} D^i \quad (18)$$

$$RMS = \sqrt{1/N\sum_{i=1}^{N}\left(\widetilde{MP_i} - MP_i\right)^2} \quad (19)$$

where $\widetilde{MP_i}$ is the reference value, MP_i denotes the value estimated by the model, and N is the number of observations.

4. Results

4.1. Validation with ERA5 Data

The 2017 ERA5 data are used to validate the CPTw model. Using a different year of ERA5 data to validate the model is necessary since this variation is free of the influences from the systematic biases between different kinds of data sets. For each grid node in the research area, we compare the ERA5 data-derived pressure, temperature, and water vapor pressure with the model outputs and calculate the bias, STD, and RMS of their differences. The results are shown in Table 1 and Figure 5.

Table 1. Validation results of the CPTw model tested by ERA5 data.

	Pressure (hPa)			Temperature (K)			Water Vapor Pressure (hPa)		
	Bias	**STD**	**RMS**	**Bias**	**STD**	**RMS**	**Bias**	**STD**	**RMS**
Mean	0.5	3.88	3.94	0.44	3.16	3.21	0	2.29	2.29
[Min	[−1.36	[1.59	[1.59	[−1.46	[0.63	[0.63	$[-4.65 \times 10^{-8}$	[0.56	[0.56
Max]	1.75]	9.84]	9.86]	2.70]	6.05]	6.06]	6.87×10^{-8}]	4.17]	4.17]

Note. STD = standard deviation; RMS = root mean square.

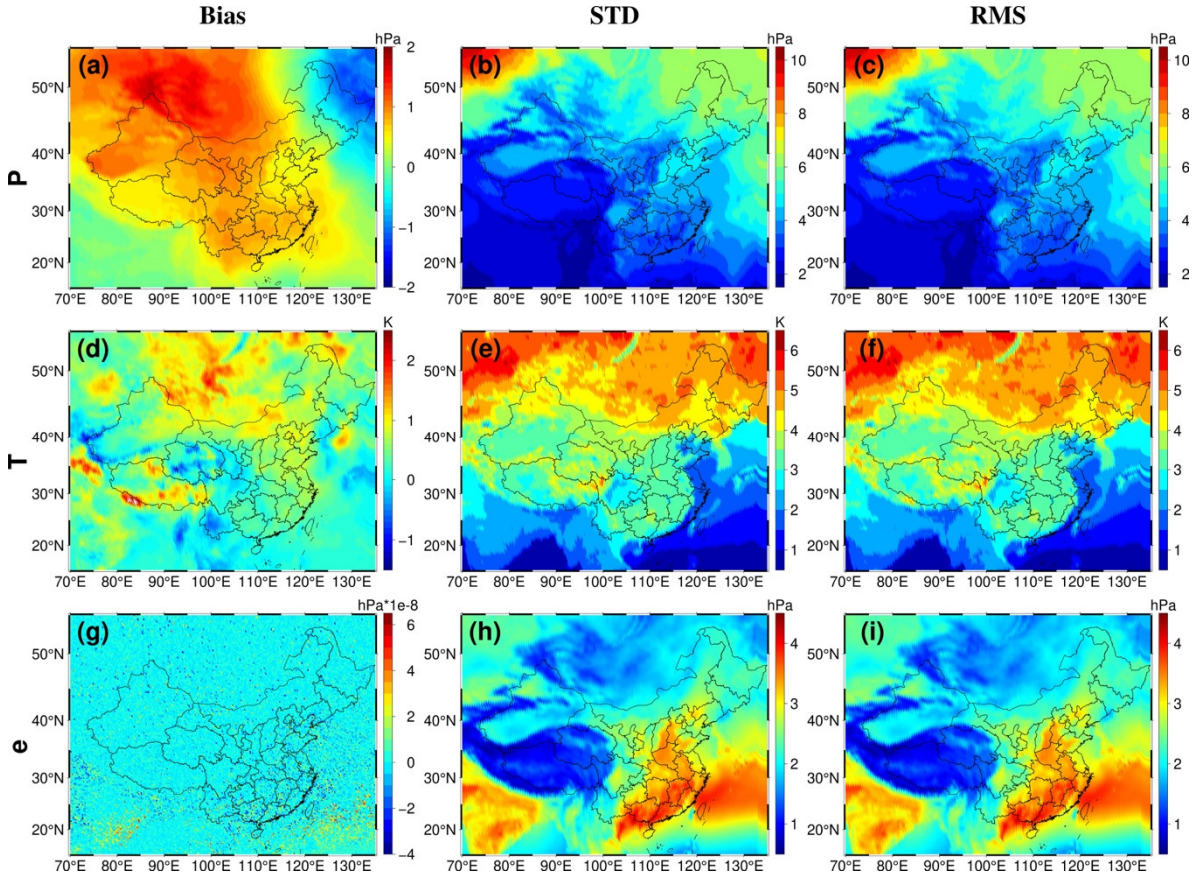

Figure 5. Bias, STD, and RMS of the pressure (**a–c**), temperature (**d–f**), and water vapor pressure (**g–i**) validated by ERA5 hourly surface 0.25° × 0.25° data in 2017.

Table 1 shows that the mean bias of pressure is 0.50 hPa with a minimum of −1.36 hPa and a maximum of 1.75 hPa, the mean RMS is 3.94 hPa, and the RMS ranges from 1.59 hPa to 9.86 hPa. Figure 5a illustrates that the pressure tends to have positive bias over the research area, except for the northeast regions. The absolute bias of pressure is biggest in the Xinjiang Province and in the northern regions, and the overall absolute bias is relatively small (0.72 hPa) in mainland China. The distributions of the STD (Figure 5b,e,h) and the RMS (Figure 5c,f,i) are similar, so only the RMS is described here. Figure 5c shows that the pressure's RMS is larger at high-latitude regions, especially in the northwestern region, and smaller at low-latitude regions, especially in Qinghai–Tibetan Plateau. This is because the pressure has stronger variations in high-latitude regions than in low-latitude regions (see Figure A1d in Appendix A for annual amplitudes of pressure). The stronger seasonal and synoptic variations bring more difficulty in modeling pressure, resulting in larger RMS. The mean RMS of pressure from the Qinghai–Tibetan Plateau is 1.75 hPa smaller than that in other regions, which is because the magnitudes and variations of pressure there are slighter than those in other regions (see Figure A1a,d in Appendix A for mean values and annual amplitudes of pressure).

The mean bias of temperature is 0.44 K with a minimum of −1.46 K and a maximum of 2.70 K, the RMS ranges from 0.63 to 6.06 K, with a mean value of 3.21 K. Figure 5d shows that the bias of temperature in northern regions is larger than that in the southern regions, especially at latitudes higher than 45°. Figure 5f shows that the RMS in high latitudes for temperature is larger than those in low latitudes, and larger on land than over the sea. This is ascribed to variations of temperature from the high-latitude regions, which are stronger than those from low-latitude regions, and stronger on the land than over the sea, which can be observed from Figure A1e in Appendix A for annual amplitudes of temperature.

The bias of water vapor pressure is close to zero in the entire research area, the RMS ranges from 0.56 hPa to 4.17 hPa with an average of 2.29 hPa. Figure 5i presents that the water vapor pressure's RMS is larger in the east, southwest of the research area, and smaller in the Qinghai–Tibetan Plateau. This results from the fact that the eastern regions are near the Pacific Ocean and the southwestern regions are close to the Indian Ocean. The influence of the East Asian monsoon and South Asian monsoon in these regions is strong. The abundance and high changes of water vapor lead to the larger RMS there (see Figure A1c,f,i in Appendix A for mean values, and annual and semiannual amplitudes of water vapor pressure). In contrast, the high altitude and the dry climate of the Qinghai–Tibetan Plateau causes very small water vapor pressure in that region (see Figure A1c in Appendix A for mean values of water vapor pressure). Figure A2 in Appendix A shows the distributions of the fitting residuals' RMS, which are in agreement with Figure 5c,f,i, demonstrating that the model accuracy and the fitting accuracy are strongly related.

To further analyze the temporal variations of the model's accuracy, we calculated the spatially averaged RMS daily and show them in Figure 6. As seen in Figure 6, the RMS of pressure has obvious seasonal features, i.e., the RMS is smaller (<3 hPa) in summer and larger (>3 hPa) in other seasons. The RMS of pressure and pressure itself show an apparent correlation, i.e., when the pressure is high its RMS is also high, and vice versa. The RMS of temperature is smaller (<2.5 K) in summer and larger (>2.5 K) in other seasons and shows anticorrelation with the temperature. As for water vapor pressure, larger RMS is observed during summer, while smaller RMS appears in winter. The RMS of water vapor pressure and water vapor pressure itself shows a positive correlation.

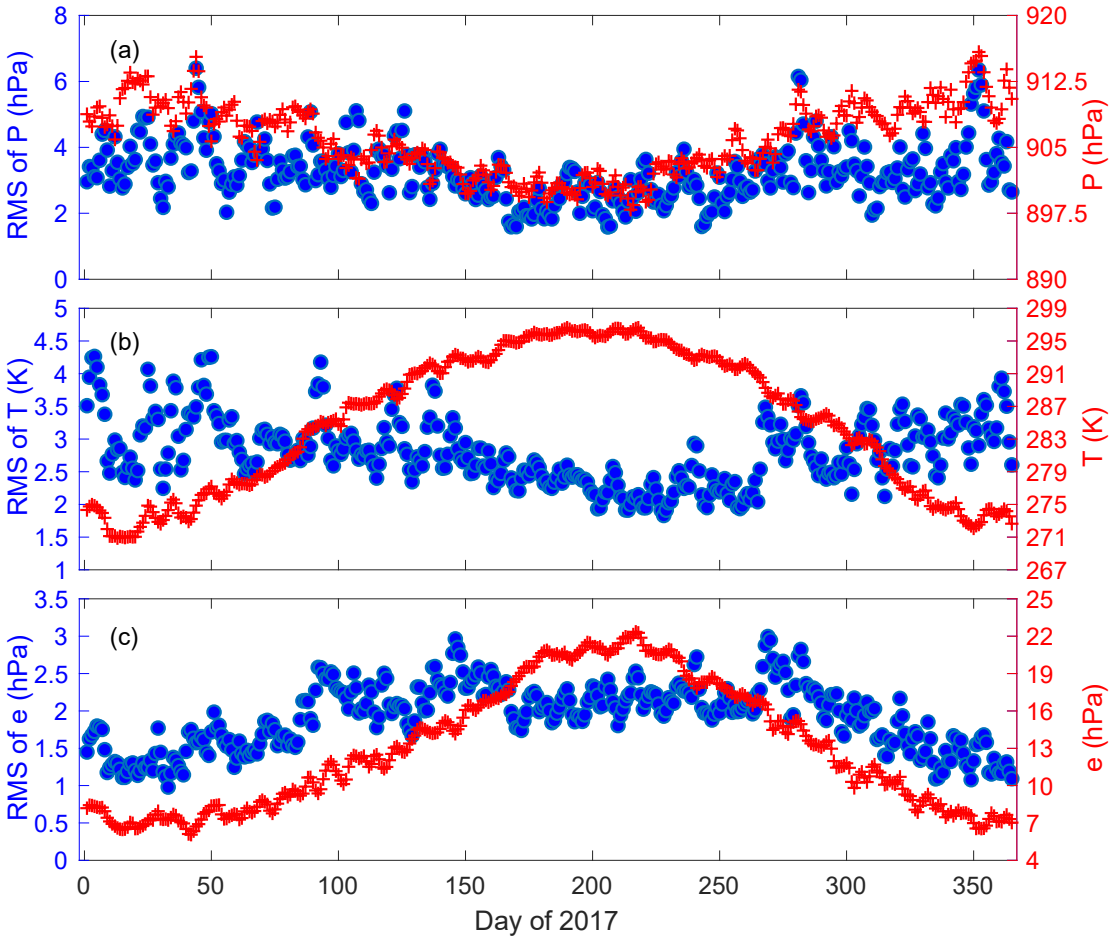

Figure 6. Time series of daily RMS of the CPTw model tested by ERA5 data in 2017. (**a**) Blue dots are daily RMS of pressure and red plus signs are daily pressure. (**b**) Blue dots are daily RMS of temperature and red plus signs are daily temperature. (**c**) Blue dots are daily RMS of water vapor pressure and red plus signs are daily water vapor pressure.

4.2. Validation with Radiosonde Data

4.2.1. Model Performance

Pressure, temperature, and water vapor pressure from 80 radiosonde stations in 2017 were used to assess the CPTw model in comparison with the commonly used GPT2w model (1° version). There are two aspects that may improve the performance of the CPTw model, one is the new data set and the other is the improved spatiotemporal resolution. To understand how the two aspects contribute to model improvements, we developed an intermediate model named CPTw_i which has the same mathematical schemes and spatiotemporal resolutions with the GPT2w model (the different part is modeling data set). This model helps to differentiate the contributions from data updating and resolution improvements. So, in this section we apply independent radiosonde data to compare the three models. Table 2 shows the accuracies of the three models.

Table 2. Accuracies of the GPT2w, CPTw, and CPTw_i models assessed by radiosonde data.

Model	Pressure (hPa)			Temperature (K)			Water Vapor Pressure (hPa)		
	Bias	**STD**	**RMS**	**Bias**	**STD**	**RMS**	**Bias**	**STD**	**RMS**
GPT2w	1.35 [−7.77, 7.12]	4.08 [1.91, 6.28]	5.25 [1.96, 9.15]	−1.06 [−4.68, 1.39]	4.51 [1.00, 7.14]	4.72 [1.09, 8.54]	0.5 [−3.86, 3.29]	2.9 [1.17, 6.08]	3.12 [1.18, 6.35]
CPTw	−0.08 [−3.54, 8.49]	3.98 [1.83, 6.27]	4.51 [2.42, 9.31]	−0.14 [−2.73, 1.61]	3.41 [0.96, 5.21]	3.5 [1.00, 5.23]	0.29 [−2.79, 2.28]	2.83 [1.19, 6.06]	2.97 [1.20, 6.14]
CPTw_i	0.39 [−3.14, 9.84]	4.08 [1.94, 6.28]	4.62 [2.30, 10.59]	0.36 [−4.17, 2.51]	4.44 [0.99, 6.81]	4.56 [1.02, 7.82]	0.46 [−2.02, 2.36]	2.86 [1.13, 6.09]	3.00 [1.18, 6.18]

Note. STD = standard deviation; RMS = root mean square.

Table 2 presents the CPTw model's mean bias, STD, and RMS for pressure, which are −0.08, 3.98, and 4.51 hPa, while they become 1.35, 4.08, and 5.25 hPa for the GPT2w model, suggesting an accuracy improvement of 14.1% in terms of RMS in the CPTw model. The CPTw model's mean bias, STD, and RMS for temperature are −0.14, 3.41, and 3.50 K, while they become −1.06, 4.51, and 4.72 K for the GPT2w model, which indicates an accuracy improvement of 25.8% in terms of RMS in the CPTw model. Furthermore, the CPTw model's mean bias, STD, and RMS for water vapor pressure are 0.29, 2.83, and 2.97 hPa, while they become 0.50, 2.90, and 3.12 hPa for the GPT2w model, suggesting an improvement of 4.8% in terms of RMS in the CPTw model. All the above point to that the CPTw model outperforms the GPT2w model in estimating pressure, temperature, and water vapor pressure.

To identify the percentages of improvements contributed from data updating (from ERA-Interim to ERA5) and resolution improvements, we first compare the performance of the GPT2w model with the CPTw_i model. The only difference between them is the data set used to build the model. Results show that the CPTw_i model's bias, STD, and RMS are overall smaller than that of the GPT2w model in estimating pressure, temperature, and water vapor pressure. When compared with the GPT2w model, the CPTw_i model has 12.0%, 3.4%, and 3.8% improvement for pressure, temperature, and water vapor pressure in terms of RMS, which are attributed to the use of ERA5 data. We then compare the CPTw_i model with the CPTw model. The only difference between the two models is the spatiotemporal resolutions (1° to 0.25°, 6 to 1 h). Results show that the CPTw model improves the model accuracy in terms of RMS by 2.4% for pressure, 23.2% for temperature, and 1.0% for water vapor pressure, which are due to improvement in the spatiotemporal resolution. When these improvements (referenced to CPTw_i) are referenced to the GPT2w model, they become 2.1%, 22.4%, and 1.0%.

The above analysis suggests that the accuracy improvement in pressure (14.1%) is mainly contributed from data updating (12.0%) and slightly from resolution improvement (2.1%). The accuracy improvement in temperature (25.8%) is mainly contributed from resolution improvement (22.4%) and slightly from data updating (3.4%). The water vapor pressure improvement (4.8%) is largely contributed from data updating (3.8%) and slightly from resolution improvement (1.0%). All these indicate data updating and resolution improvement are two important and necessary aspects for improving model performances and that they can contribute differently to the meteorological parameters.

To demonstrate the performances of different models in a more intuitive way, Figure 7 gives RMSs reduction at all radiosonde sites. It can be seen in Figure 7a that the CPTw model shows smaller pressure RMS than the GPT2w model at most stations, notably in the western regions. Figure 7b shows that the CPTw model's RMS for temperature is significantly decreased in comparison with the GPT2w model at almost all stations, and the reduction is greater in the western regions than that in other regions. Figure 7c reveals that the RMS of CPTw model for water vapor pressure is smaller than that of the GPT2w model at more than half of stations, and most of the RMS reductions appear in the western regions.

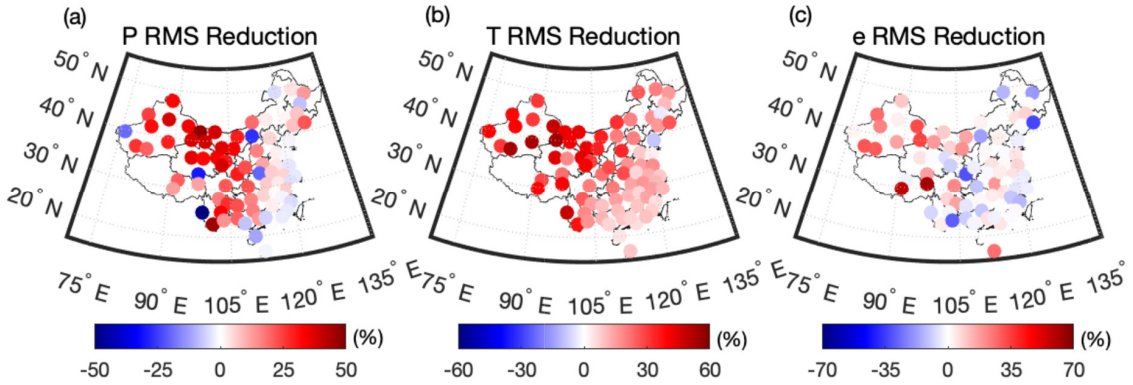

Figure 7. RMS reductions of the CPTw model compared with the GPT2w model for pressure (**a**), temperature (**b**), and water vapor pressure (**c**).

4.2.2. Spatial Distribution of Model Accuracy

To analyze the performances of the two compared models in different latitudes in China, we divide the research area into eight latitudinal bands and calculate bias, STD, and RMS within each band for the CPTw model and the GPT2w model. Figure 8 shows that STD and RMS of pressure and temperature increase with increasing latitude for both models, indicating that the accuracies of pressure and temperature are correlated with latitude. The relation between the accuracy of water vapor pressure and latitude is not obvious. These results show that the accuracy analyzed by radiosonde data is consistent with those estimated by ERA5 data (see Section 4.1).

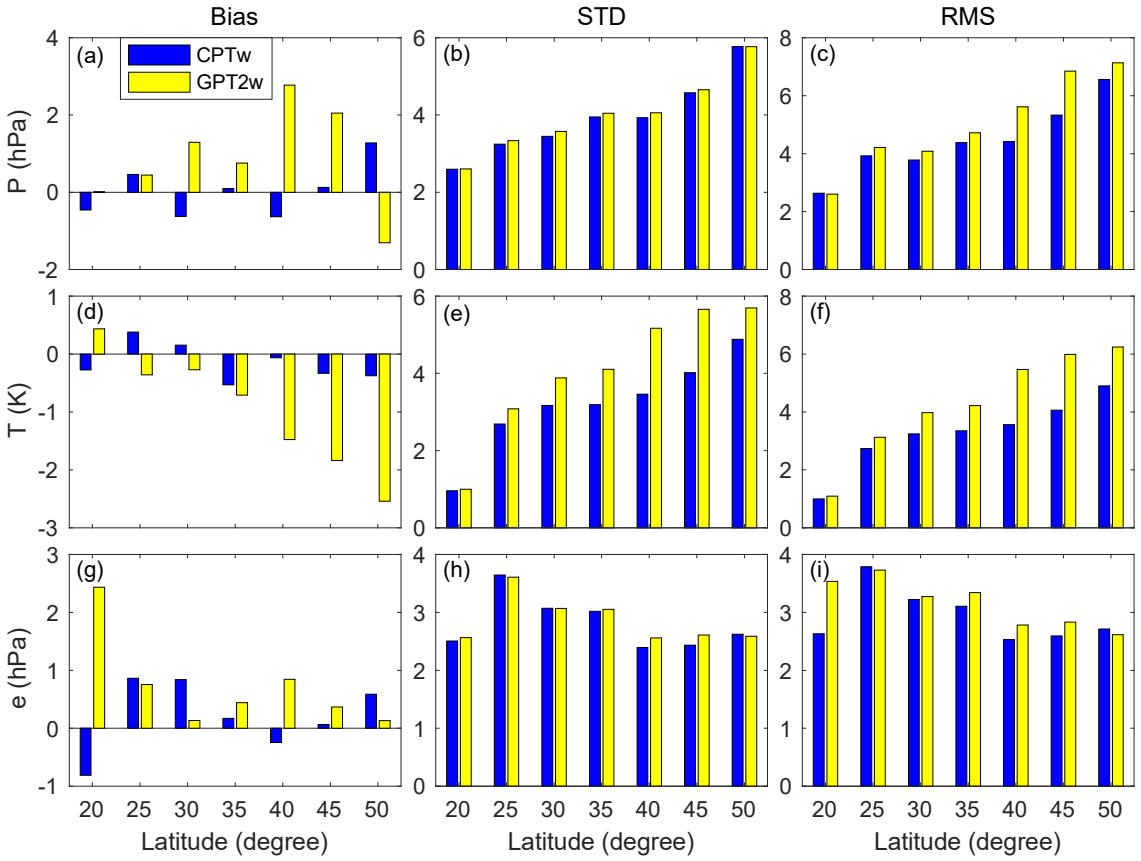

Figure 8. Bias, STD, and RMS of pressure (**a**–**c**), temperature (**d**–**f**), and water vapor pressure (**g**–**i**) from different models at different latitude ranges.

The reduction of absolute bias, STD, and RMS for the CPTw model relative to the GPT2w model at different heights is presented in Figure 9. In Figure 9, positive values mean positive accuracy improvements of the CPTw model relative to the GPT2w model. It shows that the CPTw model has smaller absolute bias and RMS for pressure than the GPT2w model, except for the heights from 100 to 250 m. This suggests that the pressure height corrections in the CPTw model perform better than that in the GPT2w model. The CPTw temperature has positive absolute bias reduction in most height intervals, except for above 2000 m, and positive RMS reduction in all height intervals. The reduction in water vapor pressure bias shows no clear trends. STD and RMS reductions for the CPTw pressure, temperature, and water vapor pressure overall increase with increasing height, suggesting that the CPTw model performs even better at greater heights.

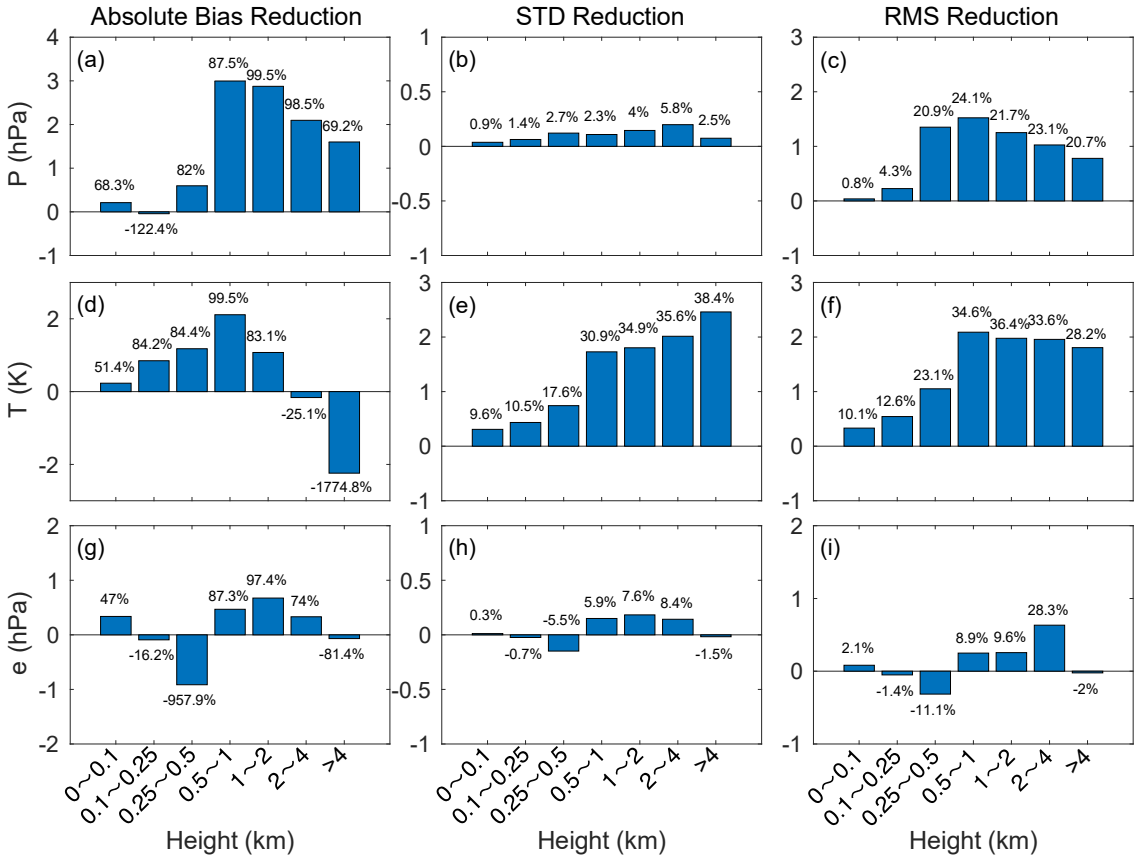

Figure 9. Absolute bias reduction, STD reduction, and RMS reduction of pressure (**a–c**), temperature (**d–f**), and water vapor pressure (**g–i**) from the CPTw model in comparison with the GPT2w model at each altitude range. (Positive values mean positive accuracy improvements in the CPTw model).

4.2.3. Model Accuracies of Different Seasons

To investigate the models' accuracies at different times, Figure 10 provides the pressure, temperature, and water vapor pressure from the CPTw model and the GPT2w model in 2017 compared with the radiosonde data at four stations Xuzhou, Hotan, Simao, and Ejin Qi. These four stations are located in the eastern, western, southern, and northern China (see Figure 1). It shows that a better consistency exists between the CPTw pressure and the radiosonde data at the four stations compared to the GPT2w model. The GPT2w model underestimates pressure for most of the time, resulting in overall a positive bias. There is a better agreement between temperature from the CPTw model and the radiosonde temperature compared to the GPT2w model. The water vapor pressure is apparently underestimated by the GPT2w model in summer, while the CPTw water vapor pressure is more consistent with the radiosonde data. In addition, the CPTw model's curves for meteorological

parameters are thicker than the corresponding curves of the GPT2w model. This result means that the CPTw model can capture high-frequency variations of meteorological parameters while the GPT2w model cannot. This is attributed to modeling of diurnal variations. Overall, the results in Figure 10 indicate that the CPTw model has more temporal stability than the GPT2w model for forecasting meteorological parameters.

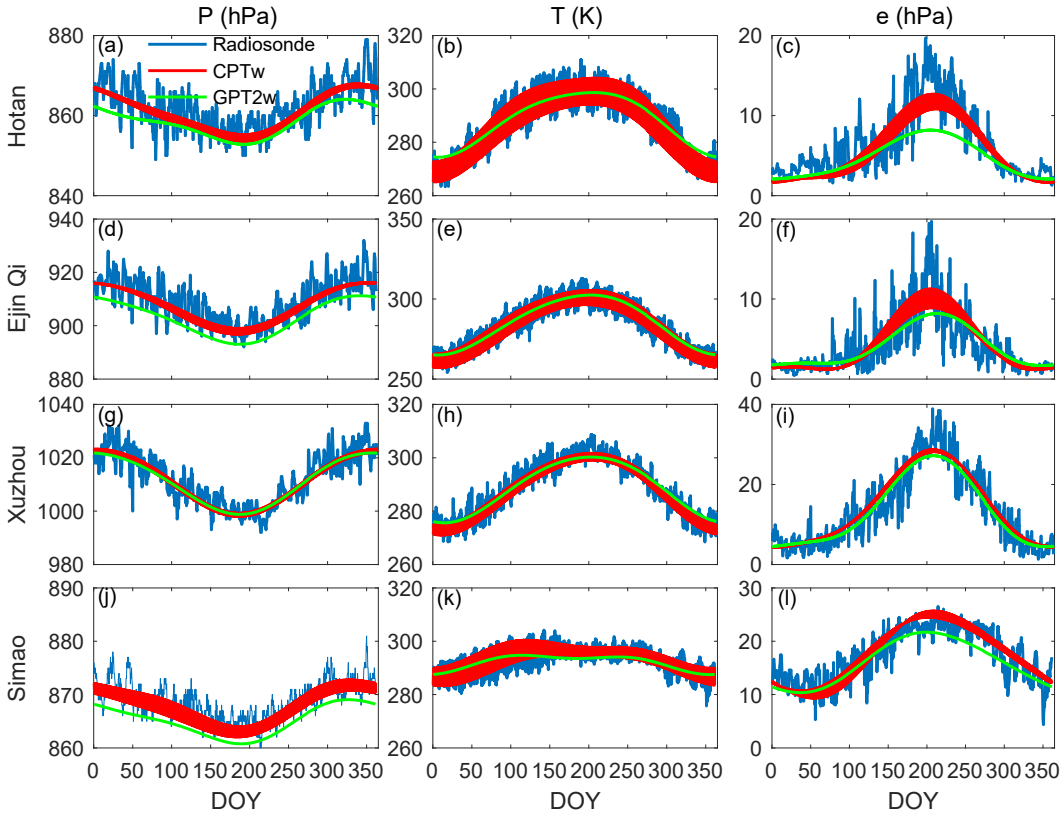

Figure 10. Pressure, temperature, and water vapor pressure at stations Hotan (**a–c**), Ejin Qi (**d–f**), Xuzhou (**g–i**), and Simao (**j–l**) from the CPTw model, the GPT2w model, and radiosonde data.

5. Conclusions

In this study, a refined regional empirical model (CPTw) is established for estimating pressure, temperature, and water vapor pressure over China and its surrounding areas. This model is based on the ECMWF ERA5 data and has greater spatial resolution (0.25° × 0.25°) and temporal resolution (1 h). By analyzing the temporal characteristics of pressure, temperature, and water vapor pressure, we find that pressure has strong diurnal and semidiurnal variations, temperature has pronounced diurnal variations, and water vapor pressure has no regular semidiurnal variations. In view of these, we build a new model that takes into account the annual, semiannual, diurnal, and semidiurnal variations in pressure, temperature, and water vapor pressure. In this new model, we also improve the height corrections via considering the annual, semiannual, diurnal, and semidiurnal variations in temperature lapse rates and water vapor pressure decrease factors.

The accuracy of the CPTw model is validated using ERA5 data—the RMS of pressure, temperature, and water vapor pressure are 3.94 hPa, 3.21 K, and 2.29 hPa. Validated by radiosonde data, the CPTw model improves the accuracy of pressure, temperature, and water vapor pressure by 14.1%, 25.8%, and 4.8% in terms of RMS when compared with the widely used GPT2w model. These improvements are benefited from better reanalysis data and improved spatiotemporal resolution. Comprehensive validations indicate a better performance of the CPTw model compared to the canonical GPT2w model, which will not only contribute to real-time GNSS positioning/navigation and GNSS meteorology but also to high precision geodetic applications.

Author Contributions: Data curation, L.L., Z.S. and X.Y.; formal analysis, Y.Y.; investigation, J.L.; methodology, J.L. and B.Z.; software, J.L. and B.Z.; validation, J.L.; writing—original draft preparation, J.L.; writing—review and editing, J.L. and B.Z.; All authors have read and agreed to the published version of the manuscript.

Funding: This work was supported by the National Natural Science Foundation of China (41704004, 41874033, 41704027, and 41664002), the China Postdoctoral Science Foundation (2018M630880, 2019T120687), the Guangxi Natural Science Foundation of China (2017GXNSFDA198016, 2017GXNSFBA198139, 2018GXNSFBA050005), the Guangxi Key Laboratory of Spatial Information and Geomatics (16-380-25-27), and the Middle-aged and Young Teachers' Basic Ability Promotion Project of Guangxi (2017KY0267).

Acknowledgments: The authors would like to thank the European Centre for Medium-Range Weather Forecasts (ECMWF) for providing ERA5 reanalysis data and the University of Wyoming for providing radiosonde data. The ERA5 reanalysis data used in this paper can be freely accessed at https://cds.climate.copernicus.eu/cdsapp#!/search?text=ERA5. The radiosonde data can be accessed at http://weather.uwyo.edu/upperair/sounding.html.

Conflicts of Interest: The authors declare no conflict of interest.

Appendix A

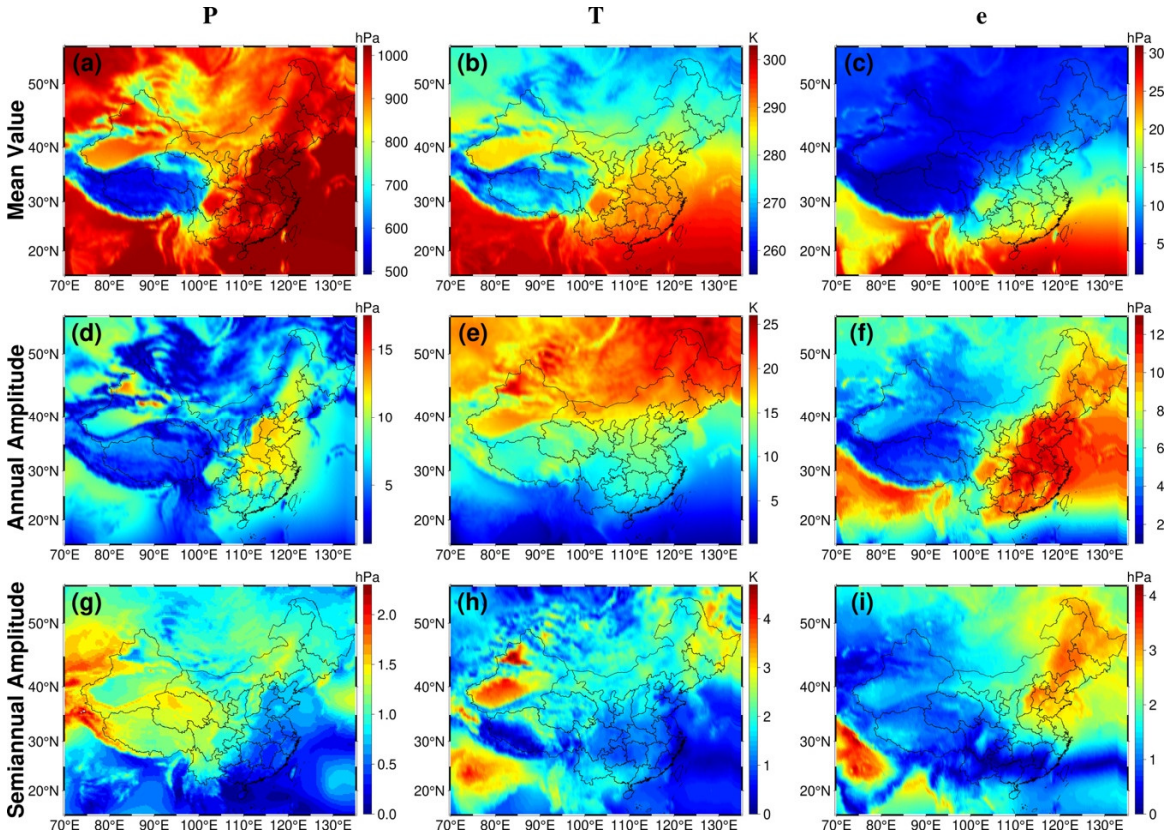

Figure A1. Mean values, annual, and semiannual amplitudes of pressure (**a,d,g**), temperature (**b,e,h**), and water vapor pressure (**c,f,i**).

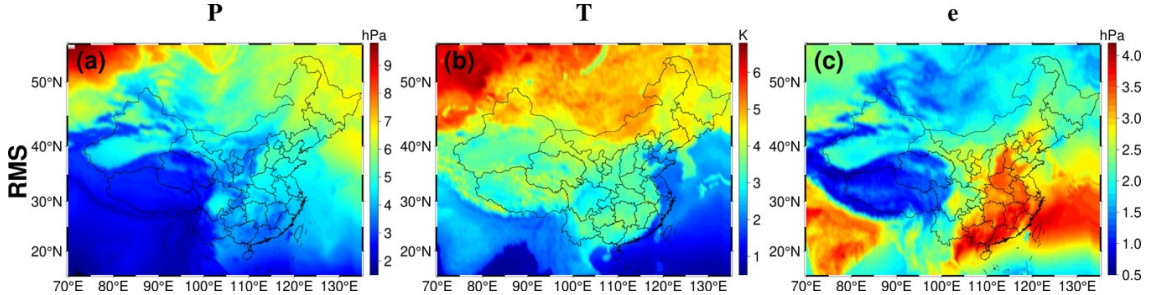

Figure A2. RMS of fitting residuals of pressure (**a**), temperature (**b**), and water vapor pressure (**c**).

References

1. Davis, J.L.; Herring, T.A.; Shapiro, I.I.; Rogers, A.E.E.; Elgered, G. Geodesy by radio interferometry: Effects of atmospheric modeling errors on estimates of baseline length. *Radio Sci.* **1985**, *20*, 1593–1607. [CrossRef]
2. Tregoning, P.; Herring, T.A. Impact of a priori zenith hydrostatic delay errors on GPS estimates of station heights and zenith total delays. *Geophys. Res. Lett.* **2006**, *33*, L23303. [CrossRef]
3. Boehm, J.; Heinkelmann, R.; Schuh, H. Short Note: A global model of pressure and temperature for geodetic applications. *J. Geod.* **2007**, *81*, 679–683. [CrossRef]
4. Saastamoinen, J.H. Atmospheric Correction for the Troposphere and the Stratosphere in Radio Ranging Satellites. *Use Artif. Satell. Geod.* **1972**, *15*, 247–251. [CrossRef]
5. Jin, S.; Park, J.U.; Cho, J.H.; Park, P.H. Seasonal variability of GPS-derived zenith tropospheric delay (1994–2006) and climate implications. *J. Geophys. Res. Atmos.* **2007**, *112*, D09110. [CrossRef]
6. Bohm, J.; Moller, G.; Schindelegger, M.; Pain, G.; Weber, R. Development of an improved empirical model for slant delays in the troposphere (GPT2w). *GPS Solut.* **2015**, *19*, 433–441. [CrossRef]
7. Bevis, M.; Businger, S.; Herring, T.A.; Rocken, C.; Anthes, R.A.; Ware, R.H. GPS meteorology: Remote sensing of atmospheric water vapor using the global positioning system. *J. Geophys. Res. Atmos.* **1992**, *97*, 15787–15801. [CrossRef]
8. Wang, X.; Zhang, K.; Wu, S.; He, C.; Cheng, Y.; Li, X. Determination of zenith hydrostatic delay and its impact on GNSS-derived integrated water vapor. *Atmos. Meas. Tech.* **2017**, *10*, 2807–2820. [CrossRef]
9. Ding, M. A neural network model for predicting weighted mean temperature. *J. Geod.* **2018**, *92*, 1187–1198. [CrossRef]
10. He, C.; Wu, S.; Wang, X.; Hu, A.; Zhang, K. A new voxel-based model for the determination of atmosphericweighted-mean temperature in GPS atmospheric sounding. *Atmos. Meas. Tech.* **2017**, *10*, 2045–2060. [CrossRef]
11. Wang, X.; Zhang, K.; Wu, S.; Fan, S.; Cheng, Y. Water vapor-weighted mean temperature and its impact on the determination of precipitable water vapor and its linear trend. *J. Geophys. Res. Atmos.* **2016**, *121*, 833–852. [CrossRef]
12. Larson, K.M. Unanticipated Uses of the Global Positioning System. *Annu. Rev. Earth Planet. Sci.* **2019**, *47*, 19–40. [CrossRef]
13. Li, W.; Yuan, Y.; Ou, J.; He, Y. IGGtrop_SH and IGGtrop_rH: Two Improved Empirical Tropospheric Delay Models Based on Vertical Reduction Functions. *IEEE Trans. Geosci. Remote Sens.* **2018**, *56*, 5276–5288. [CrossRef]
14. Kouba, J. Testing of global pressure/temperature (GPT) model and global mapping function (GMF) in GPS analyses. *J. Geod.* **2009**, *83*, 199–208. [CrossRef]
15. Petit, G.; Luzum, B. IERS Conventions. 2010. Available online: http://www.iers.org/TN36 (accessed on 1 January 2014).
16. Yao, Y.; Zhu, S.; Yue, S. A globally applicable, season-specific model for estimating the weighted mean temperature of the atmosphere. *J. Geod.* **2012**, *86*, 1125–1135. [CrossRef]
17. Yao, Y.; Zhang, B.; Yue, S.; Xu, C.; Peng, W. Global empirical model for mapping zenith wet delays onto precipitable water. *J. Geod.* **2013**, *87*, 439–448. [CrossRef]
18. Lagler, K.; Schindelegger, M.; Bohm, J.; Krasna, H.; Nilsson, T. GPT2: Empirical slant delay model for radio space geodetic techniques. *Geophys. Res. Lett.* **2013**, *40*, 1069–1073. [CrossRef]
19. Zheng, F.; Lou, Y.; Gu, S.; Gong, X.; Shi, C. Modeling tropospheric wet delays with national GNSS reference network in China for BeiDou precise point positioning. *J. Geod.* **2017**, *92*, 545–560. [CrossRef]
20. Kalita, J.Z.; Rzepecka, Z. Impact of the initial tropospheric zenith path delay on precise point positioning convergence during active conditions. *Meas. Sci. Technol.* **2017**, *28*, 045102. [CrossRef]
21. Yang, F.; Guo, J.; Meng, X.; Shi, J.; Zhou, L. Establishment and Assessment of a New GNSS Precipitable Water Vapor Interpolation Scheme Based on the GPT2w Model. *Remote Sens.* **2019**, *11*, 1127. [CrossRef]
22. Zhao, Q.; Yang, P.; Yao, W.; Yao, Y. Hourly PWV Dataset Derived from GNSS Observations in China. *Sensors* **2020**, *20*, 231. [CrossRef] [PubMed]
23. Krueger, E.; Schueler, T.; Hein, G.; Martellucci, A.; Blarzino, G. Galileo tropospheric correction approaches developed within GSTB-V1. In Proceedings of the ENC-GNSS 2004, Rotterdam, The Netherlands, 16–19 May 2004.

24. Krueger, E.; Schüler, T.; Arbesser-Rastburg, B. The standard tropospheric correction model for the European satellite navigation system Galileo. In Proceedings of the XXVIIIth General Assembly of International Union of Radio Science (URSI), New Delhi, India, 23–29 October 2005.
25. Schuler, T. The TropGrid2 standard tropospheric correction model. *GPS Solut.* **2014**, *18*, 123–131. [CrossRef]
26. Yao, Y.; Xu, C.; Shi, J.; Cao, N.; Zhang, B.; Yang, J. ITG: A New Global GNSS Tropospheric Correction Model. *Sci. Rep.* **2015**, *5*, 10273. [CrossRef] [PubMed]
27. Zhang, W.; Lou, Y.; Huang, J.; Liu, W. A refined regional empirical pressure and temperature model over China. *Adv. Space Res.* **2018**, *62*, 1065–1074. [CrossRef]
28. Hersbach, H.; Dee, D. ERA5 reanalysis is in production. *ECMWF Newsl.* **2016**, *147*, 5–6.
29. Albergel, C.; Dutra, E.; Munier, S.; Calvet, J.C.; Munoz-Sabater, J.; de Rosnay, P.; Balsamo, G. ERA-5 and ERA-Interim driven ISBA land surface model simulations: Which one performs better? *Hydrol. Earth Syst. Sci.* **2018**, *22*, 3515–3532. [CrossRef]
30. Wexler, A. Vapor pressure formulation for water in range 0 to 100°. A Revision. *J. Res. Natl. Bur. Stand. A Phys. Chem.* **1976**, *80A*, 775–785. [CrossRef]
31. Wexler, A. Vapor pressure formulation for ice. *J. Res. Natl. Bur. Stand. A Phys. Chem.* **1977**, *81A*, 5–20. [CrossRef]
32. Chen, B.; Liu, Z. A Comprehensive Evaluation and Analysis of the Performance of Multiple Tropospheric Models in China Region. *IEEE Trans. Geosci. Remote Sens.* **2016**, *54*, 663–678. [CrossRef]
33. Huang, L.; Jiang, W.; Liu, L.; Chen, H.; Ye, S. A new global grid model for the determination of atmospheric weighted mean temperature in GPS precipitable water vapor. *J. Geod.* **2019**, *93*, 159–176. [CrossRef]
34. Yao, Y.; Xu, C.; Zhang, B.; Cao, N. GTm-III: A new global empirical model for mapping zenith wet delays onto precipitable water vapour. *Geophys. J. Int.* **2014**, *197*, 202–212. [CrossRef]
35. Zhang, H.; Yuan, Y.; Li, W.; Zhang, B. A Real-Time Precipitable Water Vapor Monitoring System Using the National GNSS Network of China: Method and Preliminary Results. *IEEE J. Sel. Top. Appl. Earth Obs. Remote Sens.* **2019**, *12*, 1587–1598. [CrossRef]
36. Wang, J.; Zhang, L. Climate applications of a global, 2-hourly atmospheric precipitable water dataset derived from IGS tropospheric products. *J. Geod.* **2009**, *83*, 209–217. [CrossRef]
37. Aplin, K.L.; Williams, P.D. Meteorological phenomena in Western classical orchestral music. *Weather* **2011**, *66*, 300–306. [CrossRef]
38. Vedel, H. *Conversion of WGS84 Geometric Heights to NWP Model HIRLAM Geopotential Heights*; Danish Meteorolog. Inst.: Copenhagen, Denmark, 2000; pp. 01–11.
39. Pavlis, N.K.; Holmes, S.A.; Kenyon, S.C.; Factor, J.K. An earth gravitational model to degree 2160: EGM2008. In Proceedings of the EGU General Assembly 2008, Vienna, Austria, 13–18 April 2008.
40. Smith, W.L. Note on the relationship between total precipitable water and surface dew point. *J. Appl. Meteorol.* **1966**, *5*, 726–727. [CrossRef]
41. Dousa, J.; Elias, M. An improved model for calculating tropospheric wet delay. *Geophys. Res. Lett.* **2014**, *41*, 4389–4397. [CrossRef]
42. Askne, J.; Nordius, H. Estimation of tropospheric delay for microwaves from surface weather data. *Radio Sci.* **1987**, *22*, 379–386. [CrossRef]



© 2020 by the authors. Licensee MDPI, Basel, Switzerland. This article is an open access article distributed under the terms and conditions of the Creative Commons Attribution (CC BY) license (http://creativecommons.org/licenses/by/4.0/).